*Sensors* **2011**, *11*, 1261-1276; doi:10.3390/s110201261

OPEN ACCESS

*sensors*

**ISSN 1424-8220**

www.mdpi.com/journal/sensors

*Article*

# Preparation of Mesoporous and/or Macroporous $SnO_2$-Based Powders and Their Gas-Sensing Properties as Thick Film Sensors

**Luyang Yuan [1], Takeo Hyodo [2], Yasuhiro Shimizu [2,*] and Makoto Egashira [2]**

[1] Graduate School of Science and Technology, Nagasaki University, 1-14 Bunkyo-machi, Nagasaki 852-8521, Japan; E-Mail: d708057c@cc.nagasaki-u.ac.jp (L.Y.)

[2] Faculty of Engineering, Nagasaki University, 1-14 Bunkyo-machi, Nagasaki 852-8521, Japan; E-Mails: hyodo@nagasaki-u.ac.jp (T.H.); egashira@nagasaki-u.ac.jp (M.E.)

* Author to whom correspondence should be addressed; E-Mail: shimizu@nagasaki-u.ac.jp; Tel.: +81-95-819-2642; Fax: +81-95-819-2643.

*Received: 13 December 2010 / in revised form: 10 January 2011 / Accepted: 19 January 2011 / Published: 25 January 2011*

---

**Abstract:** Mesoporous and/or macroporous $SnO_2$-based powders have been prepared and their gas-sensing properties as thick film sensors towards $H_2$ and $NO_2$ have been investigated. The mesopores and macropores of various $SnO_2$-based powders were controlled by self-assembly of sodium bis(2-ethylhexyl)sulfosuccinate and polymethyl-methacrylate (PMMA) microspheres (*ca*. 800 nm in diameter), respectively. The introduction of mesopores and macropores into $SnO_2$-based sensors increased their sensor resistance in air significantly. The additions of $SiO_2$ and $Sb_2O_5$ into mesoporous and/or macroporous $SnO_2$ were found to improve the sensing properties of the sensors. The addition of $SiO_2$ into mesoporous and/or macroporous $SnO_2$ was found to increase the sensor resistance in air, whereas doping of $Sb_2O_5$ into mesoporous and/or macroporous $SnO_2$ was found to markedly reduce the sensor resistance in air, and to increase the response to 1,000 ppm $H_2$ as well as 1 ppm $NO_2$ in air. Among all the sensors tested, meso-macroporous $SnO_2$ added with 1 wt% $SiO_2$ and 5 wt% $Sb_2O_5$, which were prepared with the above two templates simultaneously, exhibited the largest $H_2$ and $NO_2$ responses.

**Keywords:** mesopore; macropore; meso-macropore; $SnO_2$ gas sensors; $SiO_2$; $Sb_2O_5$

---

## 1. Introduction

In recent years, the development for porous materials is been an essential objective of materials science research. This interest is the result of the progress in all fields of industry and technology [1-5]. According to the IUPAC definition, microporous materials are those with pore diameters less than 2 nm, mesoporous materials are those that have pore diameters between 2 and 50 nm, and macroporous materials are those with pores bigger than 50 nm [6]. Among them, macroporous and mesoporous silica with sufficient thermal stability has been applied to catalysts [7,8] membranes [9], adsorbents [10], chemical sensors [11] and templates for nanowires [12]. On the contrary, the poor thermal stability of non-silica mesoporous materials limits their applications. Over the past 50 years, semiconductor metal oxides such as $SnO_2$, ZnO and $In_2O_3$ have been extensively studied as gas sensing materials due to their various advantages such as the facile fabrication process of thin and thick films, low cost and high thermal stability [13,14]. Among the various metal oxides, $SnO_2$ is one of the most attractive materials for semiconductor gas sensors [13-23] operated at elevated temperatures (200–600 ℃). The gas sensing property of semiconductor gas sensors is largely dependent on various factors such as shape and size of the oxide particles [24-30]. In addition, strict control of nanostructure of the oxide powders is also quite effective in improving the gas sensing properties [31-34]. Thus, our group's efforts have so far been directed to preparing thermally stable mesoporous (m-) [15-17] and macroporous (mp-) [18,21] oxide films. However, the $H_2$ sensing properties of the m-$SnO_2$ sensors were relatively lower than expected from their large specific surface area and mp-$SnO_2$ showed rather excellent sensing properties to $H_2$. Moreover, our recent studies have demonstrated the successful preparation of thermally stable meso-macroporous (m·mp-) $SnO_2$ and the improvement of gas sensing properties by employing pellet-type sensor structures [19]. However, the mechanical strength of the m mp-$SnO_2$ pellets was not enough for long-term operation and this then became a subject for further investigation.

The present study is thus directed to developing m-, mp- and m mp-$SnO_2$ thick film sensors. The sensors were fabricated by screen-printing of their as-prepared powders, which were produced by employing sodium bis(2-ethylhexyl)sulfosuccinate (aerosol-OT, AOT) as a mesopore template and PMMA microspheres with an average diameter of 800 nm as a macropore template, and then subsequent calcination at 600 ℃ for 5 h. The effects of the addition of $SiO_2$ and $Sb_2O_5$ to m-, mp- and m mp-$SnO_2$ powders on their $H_2$ and $NO_2$ sensing properties were also examined.

## 2. Experimental Section

### *2.1. Preparation of Mesoporous and/or Macroporous $SnO_2$-Based Powders*

Various $SnO_2$-based powders with well-developed mesopores and/or macropores were prepared by a sol-gel method using $SnCl_4$ $5H_2O$ (Kishida Chem. Co., Ltd.) as a Sn source, AOT (Kishida Chem. Co., Ltd.) as a mesopore template and PMMA microspheres with an average diameter of 800 nm (MP-1600, Soken Chem. & Eng. Co., Ltd.) as a macropore template. A given amount of $SnCl_4$ $5H_2O$ (1.75 g) was mixed in 400 mL of ultra pure water together with an appropriate amount of AOT and/or PMMA microspheres. In some cases, appropriate amounts of tetraethoxysilane (TEOS, Kishida Chem. Co., Ltd.) and/or $SbCl_3$ (Kishida Chem. Co., Ltd.) were also added to the solution, in

order to prepare $SnO_2$ powders added with the given amounts of $SiO_2$ and/or $Sb_2O_5$. Then the pH value of the resulting mixture was adjusted to 8.5 by adding an aqueous solution of $NH_3$. The solid product obtained was aged in the solution at 20 ℃ for 3 days, then the resulting product was separated from the solution by centrifugation. After drying the product in an oven at 80 ℃ overnight, the resulting powder product was treated with a 0.1 mol $L^{-1}$ phosphoric acid solution for about 2 h, and the resulting product was dried in an oven at 80 ℃ overnight. The powder product resulting after pulverization is referred to as-prepared powder. The as-prepared powders were used for fabricating thick film sensors, but for the characterization tests, as-prepared powders were subjected to calcination at 600 ℃ for 5 h in air, which are the same conditions adopted for the thick film sensors after the screen-printing of a paste of as-prepared powders. The preparation conditions and compositions of all $SnO_2$-based powders obtained in this study and their abbreviations are summarized in Table 1.

**Table 1.** Preparation conditions of $SnO_2$-based powders.

| **Sensors** | | **Mesopore template (AOT) /g*** | **Macropore template (PMMA) /g*** | **Amount of MO added to $SnO_2$ (*x* or *y*)/wt%** | |
|---|---|---|---|---|---|
| **Kind of powder** | **Abbreviation** | | | **MO: $Sb_2O_5$ (using $NbCl_5$)** | **MO: $SiO_2$ (using TEOS)** |
| **Mesoporous (m-) $SnO_2$** | m-T*0S0* | 1.75 | none | none | none |
| | m-T*1S0* | | | | 1.0 |
| | m-T*1S5* | | | 5.0 | |
| **Meso-macroporous (m·mp-) $SnO_2$** | m·mp-T*1S0* | 1.75 | 0.35 | none | 1.0 |
| | m·mp-T*1S0.5* | | | 0.5 | |
| | m·mp-T*1S1* | | | 1.0 | |
| | m·mp-T*1S3* | | | 3.0 | |
| | m·mp-T*1S5* | | | 5.0 | |
| **Macroporous (mp-) $SnO_2$** | mp-T*1S0* | none | 0.35 | none | 1.0 |
| | mp-T*1S0.5* | | | 0.5 | |
| | mp-T*1S1* | | | 1.0 | |
| | mp-T*1S3* | | | 3.0 | |
| | mp-T*1S5* | | | 5.0 | |

* In 400 mL aqueous solution.

In our study, the $SnO_2$-based powders prepared using AOT or PMMA microspheres as a template are identified by using abbreviations such as m-T*x*S*y* or mp-T*x*S*y*, respectively, and the $SnO_2$-based powder prepared using both AOT and PMMA microspheres as templates is indicated as m mp-T*x*S*y*, as shown in Table 1. Here, T and S mean the addition of TEOS and $SbCl_3$ in the precursor solution, respectively, and *x* (*x* = 0, 1, 5) and *y* (*y* = 0, 1, 5) represent the added amounts of $SiO_2$ and $Sb_2O_5$ (wt%) with respect to the weight of $SnO_2$, respectively, on the basis of the expected weight of constituent oxides after calcination.

Crystal phase and crystallite size of $SnO_2$-based powders were characterized with X-ray diffraction (XRD, CuKα, Shimadzu Corp., RINT-2200). The crystallite size was calculated by using Scherrer's formula:

$$CS = 0.89\lambda/\beta\cos\theta \quad (1)$$

where λ is the wavelength of CuKα, $\beta$ is the full-width at the half-maximum of the (110) line and $\theta$ is the diffraction angle of the (110) peak. The specific surface area, pore volume and pore size distribution of $SnO_2$-based powders were measured by the BET method using a $N_2$ sorption isotherm (Micromeritics Instrument Corp., TriStar3000). Morphology of $SnO_2$-based thick films was observed by a scanning electron microscope (SEM, JEOL Ltd., JCM-5700).

### *2.2. Fabrication of Mesoporous and/or Macroporous $SnO_2$-Based Thick Film Sensors*

The as-prepared $SnO_2$-based powder was mixed with a printing oil which is composed of an alkyl ester of methacrylic acid as a binder, a toluene-based solvent, and an ammonium salt of polyacrylic acid as a plasticizer, and the resulting paste was screen printed on an alumina substrate, on which a pair of interdigitated Pt electrodes (gap between electrodes: 130 μm) had been printed (the thickness of the film was controlled to be about 20 μm after calcination for all the sensors fabricated). Then the printed film was subjected to heat treatment at 600 ℃ for 5 h in air prior to response measurements. The gas-sensing properties of the thick film sensors to 1,000 ppm $H_2$ and 1 ppm $NO_2$ balanced with air were measured in the temperature range of 350–500 ℃. The magnitude of the gas response was defined as the ratio ($R_a/R_g$) of the sensor resistance in air ($R_a$) to that in a target gas ($R_g$) for $H_2$, but the reverse ratio ($R_g/R_a$) was used for $NO_2$.

## 3. Results and Discussion

### *3.1. Characterization of Mesoporous and/or Macroporous $SnO_2$-Based Powders*

Pore size distribution and specific surface area (SSA) of representative m-$SnO_2$, mp-$SnO_2$ and m mp-$SnO_2$ powders after calcination are shown in Figure 1. As shown in Figures 1(a-i), m-T*0S0* powder, which was prepared only with the addition of AOT, showed a SSA of 150.9 $m^2\ g^{-1}$ and a larger pore volume of 0.153 $cm^3\ g^{-1}$ with a pore diameter of ca. 3.1 nm at the maximum pore volume (hereafter, it will be referred to as the maximum pore diameter). The characterization data of representative $SnO_2$-based powders is summarized in Table 2. The addition of 1 wt% $SiO_2$ to m-T*0S0* induced a slight increase in SSA (162.3 $m^2\ g^{-1}$) and reduced the maximum pore diameter to ca. 2.7 nm (see m-T*1S0*). This result implies the repression of growth of $SnO_2$ crystallites and/or grains by the added $SiO_2$, as was reported by Fukuoka *et al*. [12]. Simultaneous addition of 1 wt% $SiO_2$ and 5 wt% $Sb_2O_5$ to m-T*0S0* resulted in further increase in SSA slightly to a value of 176.5 $m^2\ g^{-1}$ (see m-T*1S5*). Thus, the addition of $Sb_2O_5$ was suggested to be also effective in controlling grain growth, which will be confirmed by the change in $SnO_2$ crystallite size discussed later.

It was revealed that the introduction of macropores into m-T*1S5* was very effective for increasing SSA to a value of 262.7 $m^2\ g^{-1}$ (see m mp-T*1S5*, Figures 1(c-ii)). This arises undoubtedly from the decrease in the maximum pore diameter and the increase in pore volume, as summarized in Table 2. On the other hand, the introduction of macropores only (mp-T*1S5*), instead of mesopores (m-T*1S5*), into $SnO_2$-based powder reduced SSA to a value of 112.0 $m^2\ g^{-1}$ (compare Figure 2(b-ii) with Figure 2(a-iii)) and then decreased pore volume (see Table 2). From these results, it is confirmed that the introduction of mesopores is essential for obtaining both large specific surface and large pore volume of $SnO_2$-based powders.

**Figure 1.** Pore size distributions and specific surface area of representative **(a)** m-$SnO_2$, **(b)** mp-$SnO_2$ and **(c)** m mp-$SnO_2$ powders.

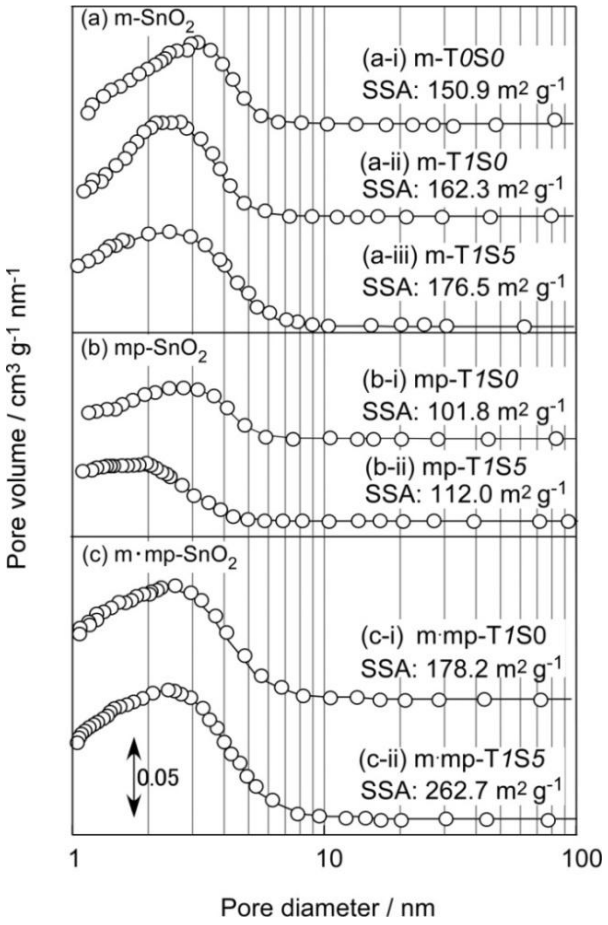


**Table 2.** Characterization data of representative m-$SnO_2$, mp-$SnO_2$ and m·mp-$SnO_2$ powders.

| Sensors | | Specific surface area (SSA) /$m^2$ $g^{-1}$ | Pore volume /$cm^3$ $g^{-1}$ | Maximum pore diameter * /nm | Crystallite size (CS) /nm |
|---|---|---|---|---|---|
| **Kind of powder** | **Abbreviation** | | | | |
| **m-$SnO_2$** | m-T*0S0* | 150.9 | 0.153 | 3.1 | 7.0 |
| | m-T*1S0* | 162.3 | 0.160 | 2.7 | 3.8 |
| | m-T*1S5* | 176.5 | 0.155 | 2.5 | 3.2 |
| **m·mp-$SnO_2$** | m·mp-T*1S0* | 178.2 | 0.184 | 2.5 | 4.2 |
| | m·mp-T*1S5* | 262.7 | 0.191 | 2.3 | 3.2 |
| **mp-$SnO_2$** | mp-T*1S0* | 101.8 | 0.090 | 2.9 | 3.9 |
| | mp-T*1S5* | 112.0 | 0.079 | 2.0 | 2.7 |

* Pore diameter at the maximum pore volume in the pore size distribution curve.

Figure 2 shows variations in SSA of representative $SnO_2$-based powders with amount of $Sb_2O_5$ added. The effect of the $Sb_2O_5$ on SSA can be seen more clearly from this figure. As for the cases of m-T*1Sy* and mp-T*1Sy* series, SSA values increased slightly with increasing amounts of $Sb_2O_5$ added, but only for the m mp-T*1Sy* series, it is obvious that SSA increased markedly with an increase in the additive amount of $Sb_2O_5$ reaching the largest value of 262.7 $m^2$ $g^{-1}$ obtained in the present study. The

reason for this preferable effect for sensor application observed only the m mp-T*1Sy* series is not yet clarified and is a subject for future work.

**Figure 2.** Variations in specific surface area of representative $SnO_2$-based powders with amounts of $Sb_2O_5$ added.

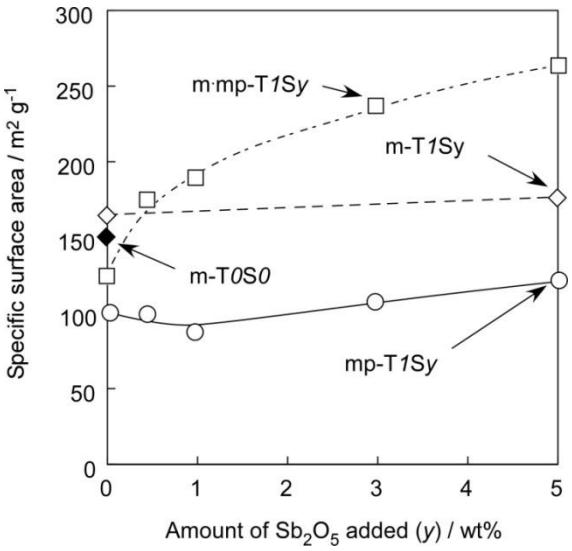


Figure 3 shows the SEM images of the fracture surface of m-T*1S5*, mp-T*1S5* and m mp-T*1S5* thick film sensors. No formation of macropores in m-T*1S5* is reasonable, since no PMMA microspheres were added, as shown in Figure 3(a). But, Figure 3(b,c) confirm the formation of many spherical macropores originating from the morphology of PMMA microspheres as a template in the mp-T*1S5* and m mp-T*1S5* thick film sensors. However, the diameter of macropores observed was in the 400–750 nm range, which was smaller than that of the diameter of raw PMMA microspheres, due to shrinkage of resulting voids during the growth of $SnO_2$ crystallites.

**Figure 3.** SEM images of fracture surface of **(a)** m-T*1S5*, **(b)** mp-T*1S5* and **(c)** m mp-T*1S5* thick film sensors.

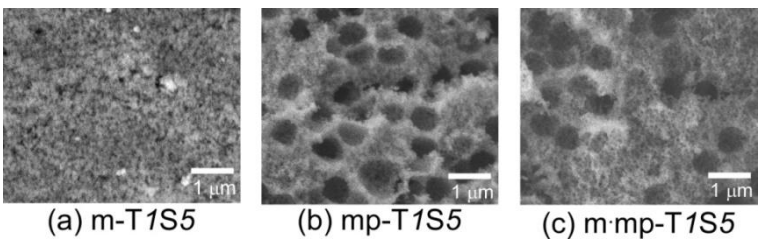


As shown in Figure 1 and Table 1, mp-$SnO_2$ powder prepared in the present study showed relatively larger SSA than the conventional $SnO_2$ powder (8.4 $m^2$ $g^{-1}$, [35]), indicating the formation of a certain amount of mesopores, irrespective of the addition or not of AOT as a mesoporous structure template. This result implies penetration or diffusion of PMMA fragments into the dried $SnO_2$ precursor material during the calcination and such fragments may act as a mesoporous template at the interface between the PMMA microsphere and surrounding dried $SnO_2$ precursor. Thus, after the calcination at 600 ℃ for 5 h of the mp-$SnO_2$ thick film, a thin mesoporous layer may be formed at the interface between the

pores and $SnO_2$ particles, as shown schematically in Figure 4(a) [36]. As for m mp-$SnO_2$, it is considered that mesopores are formed uniformly inside all the $SnO_2$ particles and the whole thick film structure, as shown in Figure 4(b).

**Figure 4.** Schematic drawing of formation mechanism of mesopores and macropores in **(a)** mp-$SnO_2$ and **(b)** m mp-$SnO_2$ thick film sensors.

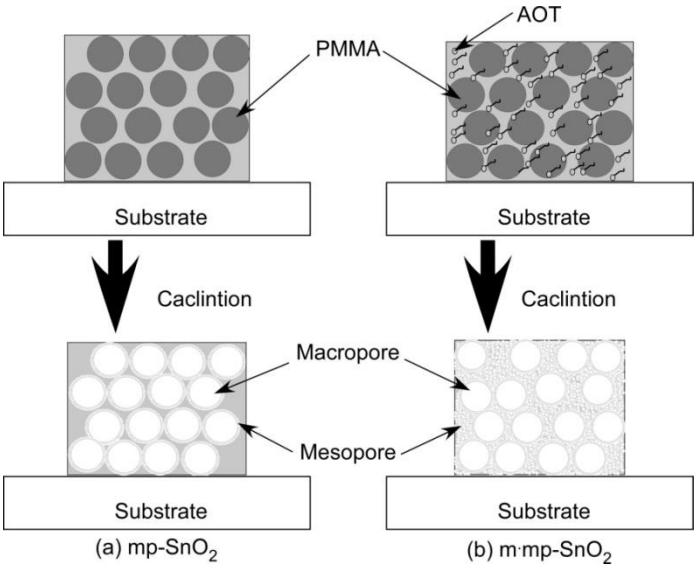


Another notable finding in Figure 3 is a relatively longer distance of the macropores in m mp-T*1S5* than that in mp-T*1S5*. Since AOT was used as a mesoporous template in fabricating m mp-$SnO_2$ powder, thermal decomposition and subsequent firing along with generation of combustion gases may induce sponge and/or bulky structure with mesopores, leading to a longer distance of the macropores, as also shown schematically in Figure 4(b).

Figure 5 shows XRD patterns of representative m-$SnO_2$, mp-$SnO_2$ and m mp-$SnO_2$ powders. Diffraction peaks of all powders were rather broad, indicating low crystallinity, but all peaks could be ascribed to those of tetragonal $SnO_2$. The CS value which was calculated for each powder using Scherrer's formula is summarized in Table 2. Variations in CS of representative $SnO_2$-based powders are shown Figure 6. On the whole, the CS values were small and were in a range of 2.7–7 nm in diameter, due to the limitation of crystallite growth induced by the phosphoric acid treatment before the calcination [15,16]. Exceptionally, m-T*0S0* showed the largest CS value of 7 nm. The CS value was decreased drastically to 3.8 nm by the addition of 1 wt% $SiO_2$ to m-T*0S0* (see m-T*1S0* in Table 2 and Figure 6). Thus, the repression of the growth of $SnO_2$ crystallites by the added $SiO_2$ could be confirmed from these results [37]. As for the powders containing 1 wt% $SiO_2$, CS values were almost comparable, whereas they tended to decrease slightly with increasing amounts of the $Sb_2O_5$ additive in each series. In addition, the kind of porous structure, *i.e.*, mesopore, macropore, and mesopore plus macropore, was found to have only a little effect on controlling the CS values. Thus, we can confirm again that the addition of 1 wt% $SiO_2$ was the most powerful method in reducing the CS value among several factors. The CS values decreased slightly by the $Sb_2O_5$ addition in each series, but no diffraction peaks other than $SnO_2$ were observed in XRD patterns even for the cases of 5 wt% $Sb_2O_5$ addition (Figure 5). This implies that Sb ions added were sufficiently incorporated into the $SnO_2$

crystal lattice and this solid-solution is also effective for the repression of the crystal growth among $SnO_2$-based crystallites [23,38,39]. These results demonstrate that the pore size distribution, SSA and CS values of $SnO_2$-based powders can be controlled by selecting the kinds of templates, the kind of additives and their additive amounts.

**Figure 5.** XRD patterns of **(a)** m-$SnO_2$, **(b)** mp-$SnO_2$ and **(c)** m mp-$SnO_2$ powders.

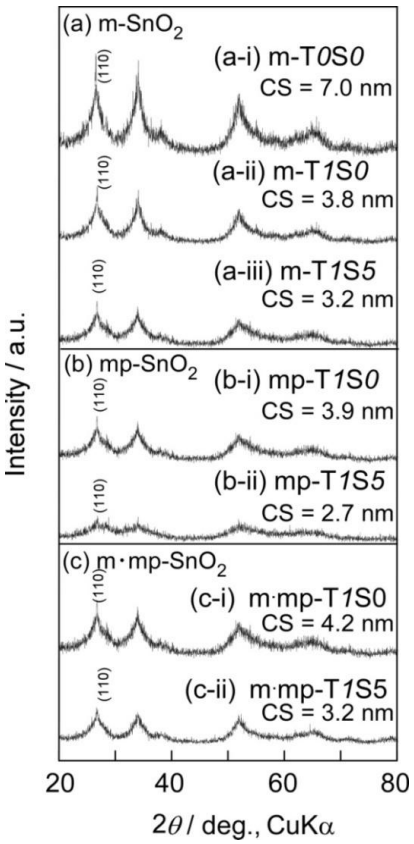


**Figure 6.** Variations in crystallite size of representative $SnO_2$-based powders with amounts of $Sb_2O_5$ added.

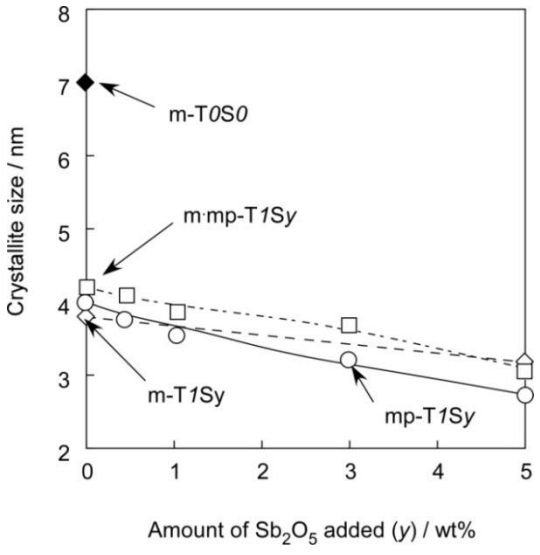

### *3.2. $H_2$ and $NO_2$ Sensing Properties of Mesoporous and/or Macroporous $SnO_2$-Based Sensors*

Variations in sensor resistance of $SnO_2$-based thick film sensors in air at 450 ℃ with amounts of $Sb_2O_5$ added are shown in Figure 7. The m-T*0S0* sensor showed the lowest resistance in air, but the addition of 1 wt% $SiO_2$ to m-T*0S0* increased the sensor resistance in air (see m-T*1S0*). The sensor resistance of other two series sensors, *i.e.*, mp-T*1S0* and m mp-T*1S0*, in air was also very high. Even if $Si^{4+}$ ions would be substituted for $Sn^{4+}$ ion sites, no valency control effect could be expected. Therefore, $SiO_2$ added was anticipated to be segregated among $SnO_2$ crystallites and/or grains and then to reduce electronic conduction of $SnO_2$-based thick film sensors, although the segregation of $SiO_2$ was not confirmed by the XRD measurements due to its small amount added.

**Figure 7.** Variations in sensor resistance of $SnO_2$-based thick film sensors in air at 450 ℃ with amounts of $Sb_2O_5$ added.

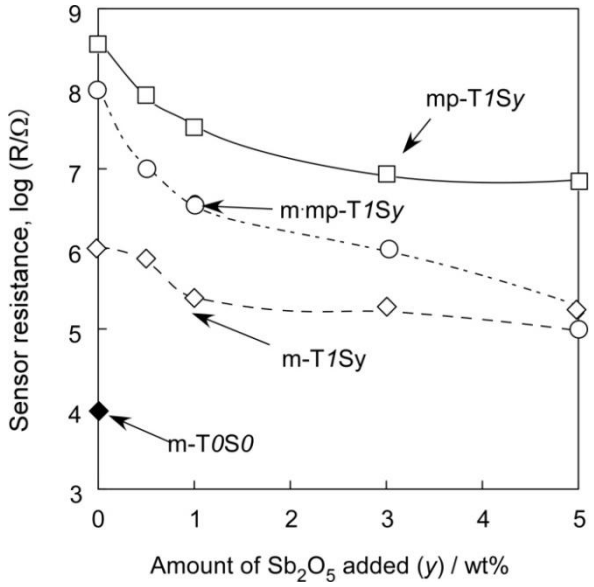


Introduction of macropores into $SnO_2$ by using PMMA microspheres (see mp-T*1Sy* series), instead of the introduction of mesopores, and/or the simultaneous introduction of macropores (see m mp-T*1Sy* series) also resulted in an increase in sensor resistance. This phenomenon can be considered to arise mainly from the introduction of air voids, which are electrical insulators, via various pores in the thick film sensors, but the mp-T*1Sy* sensor with macropores showed the largest resistance in air, irrespective of the smallest pore volume, among three series of sensors. This fact implies the existence of another factor, besides the pore volume, in determining the sensor resistance in air, such as the manner of distribution of pores in the thick film and so on, though the details are not clear at present.

In each sensor series, the sensor resistance in air decreased with increasing amounts of $Sb_2O_5$ additive. This behavior can be explained by the valency control, *i.e.*, partial substitution of $Sn^{4+}$ sites with $Sb^{5+}$ ions, producing free electrons, as described in Equation (2) [38-40]:

$$Sb_2O_5 \rightarrow 2\ Sb_{Sn} + 4\ O_O^{x} + 1/2\ O_2\ (g) + 2\ e' \quad (2)$$

These results also confirm the existence of substituted $Sb^{5+}$ ions, *i.e.*, the solid-solution of between $Sb_2O_5$ and $SnO_2$ and then little amount of segregated $Sb_2O_5$ among $SnO_2$-based particles.

Figures 8 and 9 show temperature dependence of response of $SnO_2$-based thick film sensors to 1,000 ppm $H_2$ balanced with air and 1 ppm $NO_2$ balanced with air. Almost all sensors showed the maximum response to 1,000 ppm $H_2$ at a temperature of 450 ℃. In contrast, the response to 1 ppm $NO_2$ of all sensors tended to increase as the operating temperature decreased, and showed the largest response in the temperature range studied at 350 ℃.

**Figure 8.** Temperature dependence of response $SnO_2$-based thick film sensors to 1,000 ppm $H_2$.

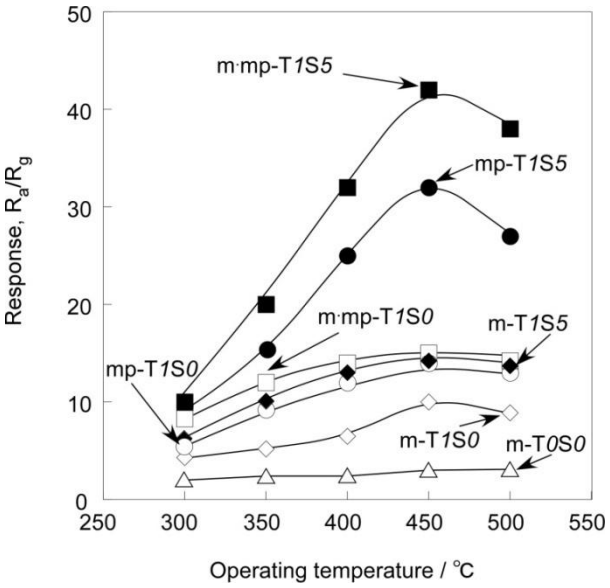


**Figure 9.** Temperature dependence of response $SnO_2$-based thick film sensors to 1 ppm $NO_2$.

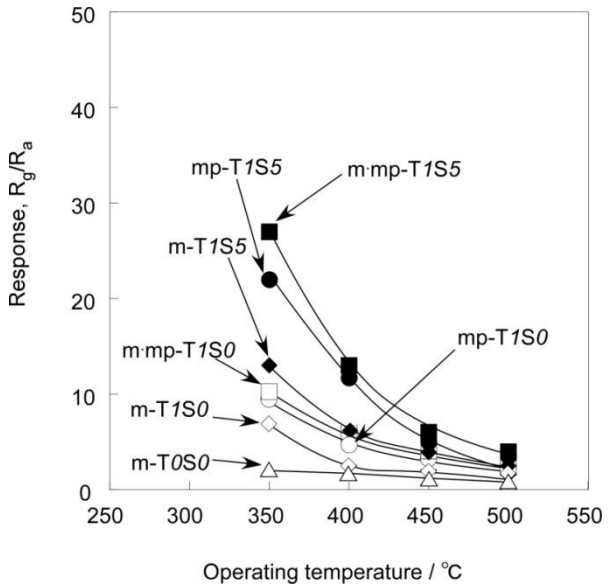


Response transients of $SnO_2$-based thick film sensors to 1,000 ppm $H_2$ at 450 ℃ and 1 ppm $NO_2$ at 350 ℃ balanced with air are shown in Figures 10 and 11, respectively. In this study, 50% response time is defined as a period necessary to achieve 50% of resistance value of $R_a - R_g$, while 50% recovery time is defined as that necessary to achieve 50% of resistance value of $R_g - R_a$ for $H_2$.

The 50% response and recovery times to $NO_2$ are also defined in the similar manner, but by using $R_g - R_a$ for response time and $R_a - R_g$ for recovery time. Hereafter, they are simply expressed as response time and recovery time, respectively. Response and recovery times of $SnO_2$-based thick film sensors to 1,000 ppm $H_2$ at 450 ℃ and 1 ppm $NO_2$ at 350 ℃ were summarized in Table 3. The m-T*0S0* sensor showed the longest response and recovery times to $H_2$ among the sensors listed in Table 3. The simultaneous addition of 1 wt% $SiO_2$ and 5 wt% $Sb_2O_5$ to m-T*0S0* was found to shorten slightly response and recovery times to $H_2$ (see m-T*1S5*).

**Figure 10.** Response transients of $SnO_2$-based thick film sensors to 1,000 ppm $H_2$ in air at 450 ℃.

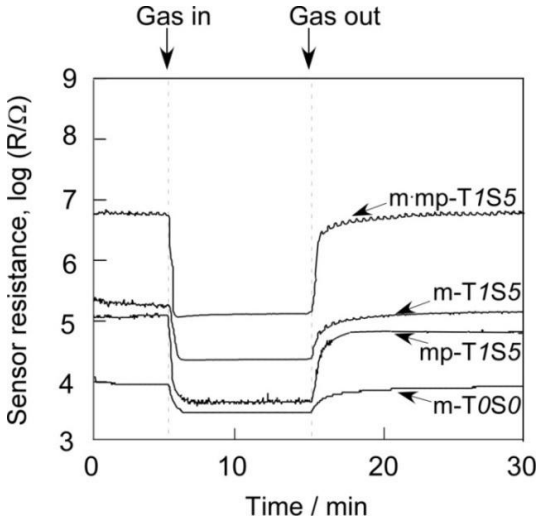


**Figure 11.** Response transients of $SnO_2$-based thick film sensors to 1 ppm $NO_2$ in air at 350 ℃.

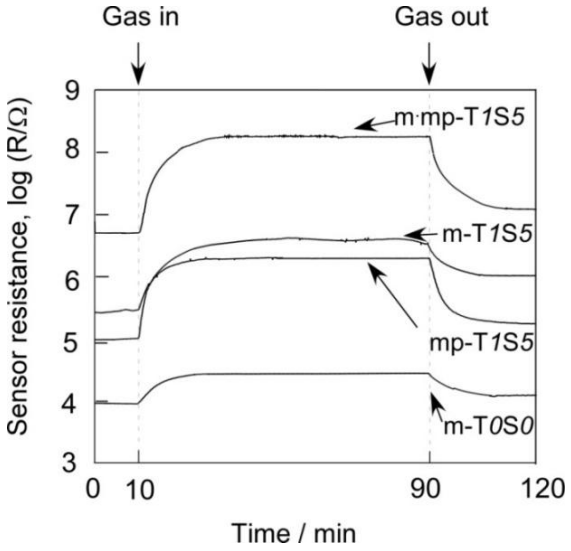


However, the m-T*1S5* sensor showed longer response and recovery times to 1 ppm $NO_2$ than m-T*0S0*. Thus, the effect of additive on the response and recovery times varied with the kind of target gas. The introduction of macropores into m-T*1S5* shortens the response and recovery times to $H_2$. More remarkable shortening of the recovery time to $H_2$ as well as response and recovery times to $NO_2$ were observed with m mp-T*1S5*. It is reasonable to consider that the response time to $H_2$ is closely

related to the diffusivity of $H_2$, while the recovery time is controlled by the diffusivity of $O_2$ which has a larger molecular size than $H_2$. As for $NO_2$, on the other hand, both the response and recovery times are considered to affected by the diffusivity of $NO_2$ itself, which has a larger molecular size than $H_2$, from its gas sensing mechanism. Such considerations predict a shorter recovery time to $H_2$ as well as shorter response and recovery times to $NO_2$ by the introduction of macropores into the sensor materials. The results obtained with m mp-T*1S5* were in good agreement with this prediction. Thus, the mp-T*1S5* sensor, which was fabricated only by the introduction of macropores, showed the fastest response to $H_2$ as well as the fastest response and recovery times to $NO_2$ among the sensors tested. But, the reason for the longer recovery time to $H_2$ of mp-T*1S5* than m mp-T*1S5* is not clear at present. Anyway, such behavior undoubtedly arises from more easy diffusion of a target gas as well as oxygen through mesopores rather than macropores. On the other hand, all of the response and recovery times to $NO_2$ are much longer than those to $H_2$. This may arise not only from slow diffusivity of $NO_2$ in comparison to $H_2$, but also from slow adsorption rate and strong interaction of $NO_2^-$ species on the oxide surface.

**Table 3.** 50% response time and 50% response time of $SnO_2$-based thick film sensors to 1,000 ppm $H_2$ at 450 ℃ and 1 ppm $NO_2$ at 350 ℃ balanced with air.

| **Sensors** | | **1,000 ppm $H_2$ (450 ℃)** | | **1 ppm $NO_2$ (350 ℃)** | |
|---|---|---|---|---|---|
| **Kind of powder** | **Abbreviation** | **50% response time/s** | **50% recovery time/s** | **50% response time/s** | **50% recovery time/s** |
| **m-$SnO_2$** | m-T*0S0* | 25 | 35 | 182 | 330 |
| | m-T*1S5* | 22 | 29 | 195 | 600 |
| **m·mp-$SnO_2$** | m·mp-T*1S5* | 20 | 17 | 154 | 325 |
| **mp-$SnO_2$** | mp-T*1S5* | 16 | 22 | 110 | 220 |

Figures 12 and 13 show variations in responses of $SnO_2$-based sensors to 1,000 ppm $H_2$ at 450 ℃ and to 1 ppm $NO_2$ at 350 ℃ in air with amounts of $Sb_2O_5$ added, respectively. From these figures, it is also apparent that the m-T*0S0* sensor showed the smallest responses to both $H_2$ and $NO_2$ among the sensors studied. The addition of 1 wt% $SiO_2$ to m-T*0S0* enhanced responses to both $H_2$ and $NO_2$ to a certain level for every series of sensors. In addition, $H_2$ and $NO_2$ responses increased with increasing amounts of $Sb_2O_5$ additive in each series of sensors. On the whole, the magnitude of the response was in the order of m mp-T*1Sy* > mp-T*1Sy* > m-T*1Sy*, when the comparison was made at the same additive amount of $Sb_2O_5$, with only one exception observed for the $NO_2$ response of the m mp-T*1S0* sensor. It is worth noting that the mp-T*1Sy* series sensors showed higher $H_2$ and $NO_2$ responses than those of m-T*1Sy* series sensors, irrespective of their smaller surface area. This implies that all the surface of sensor materials including the inner surface of mesopores is not utilized effectively for gas detection, and that easy diffusion of a target gas as well as oxygen to the active surface, *i.e.*, the existence of certain amounts of macropores inside the thick film sensors, is more important for improving gas response. The highest $H_2$ and $NO_2$ responses observed with the m mp-T*1Sy* sensors may be a result of good combination of mesopore and macropores in the thick film sensors. From these results, it was revealed that the strict control of microstructure having well-developed mesoporous and macroporous

is indispensable to enhancing gas reactivity and diffusivity and thus to improving responses to $H_2$ and $NO_2$ in air.

**Figure 12.** Variations in response of $SnO_2$-based sensors to 1,000 ppm $H_2$ in air at 450 ℃ with amounts of $Sb_2O_5$ added.

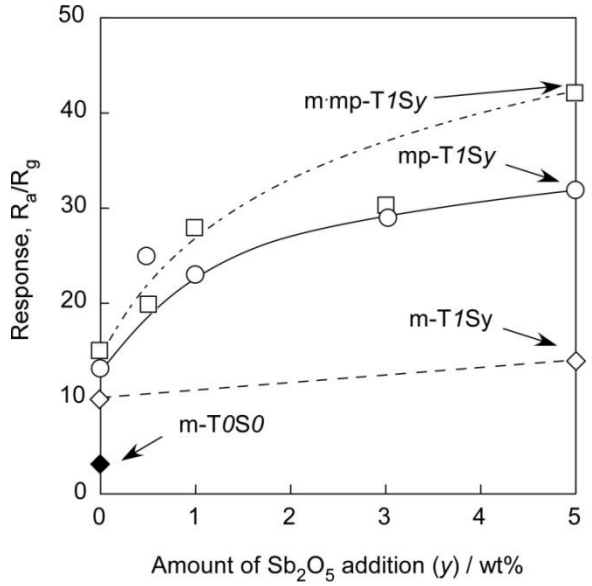


**Figure 13.** Variations in response of $SnO_2$-based sensors to 1 ppm $NO_2$ in air at 350 ℃ with amounts of $Sb_2O_5$ added.

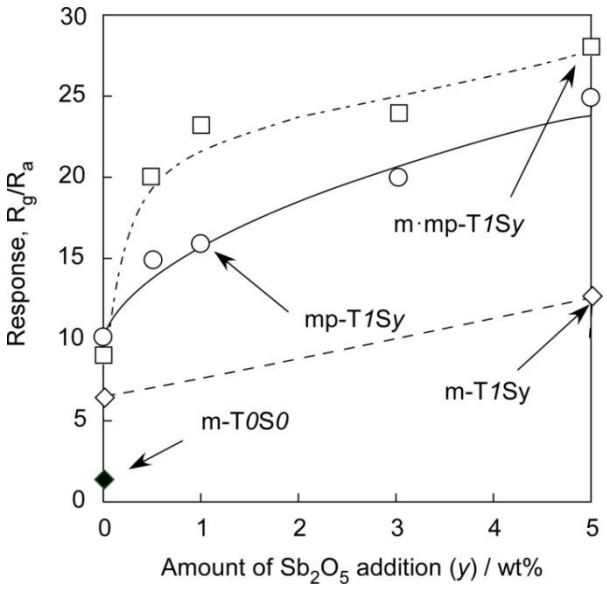


## 4. Conclusions

Mesoporous and/or macroporous $SnO_2$-based powders have been prepared by a sol-gel method by employing $SnCl_4$ $5H_2O$, ATO as a mesopore template, PMMA microspheres as a macropore template, and their gas-sensing properties as thick film sensors towards 1 ppm $NO_2$ as well as 1,000 ppm $H_2$ in air have been investigated. The addition of $SiO_2$ into mesoporous and/or macroporous $SnO_2$ was found to increase SSA of mesoporous $SnO_2$. However, the SSA of all samples increased and their CS tended

to decrease slightly with the addition of the $Sb_2O_5$. The additions of $SiO_2$ and $Sb_2O_5$ into mesoporous and/or macroporous $SnO_2$ were found to improve the sensing properties of the resulting sensors. The addition of $SiO_2$ into mesoporous and/or macroporous $SnO_2$ was found to increase the sensor resistance in air. However, the doping of $Sb_2O_5$ into mesoporous and/or macroporous $SnO_2$ was found to markedly reduce the sensor resistance in air, and to increase the response to 1,000 ppm $H_2$ as well as 1 ppm $NO_2$ in air. Among all the sensors tested, meso-macroporous $SnO_2$ mixed with 1 wt% $SiO_2$ and 5 wt% $Sb_2O_5$, which were prepared with above two templates simultaneously, exhibited the largest $H_2$ and $NO_2$ responses.

**References and Notes**


1. Soler-Illia, G.J.A.A.; Sanchez, C.; Lebeau, B.; Patarin, J. Chemical strategies to design textured materials: From microporous and mesoporous oxides to nano networks and hierarchical structures. *Chem. Rev.* **2002**, *102*, 4093-4138.
2. Havancsak, K. Materials science: Testing and informatics I. *Materi. Sci. Forum* **2003**, *85*, 414-415.
3. Wolf, E.L. *Nanophysics and Nanotechnology*: *An Introduction to Modern Concepts in Nanoscience*; John Wiley & Sons: New York, NY, USA, 2004.
4. Yamazoe, N. New approaches for improving semiconductor gas sensors. *Sens. Actuat. B* **1991**, *5*, 7-19.
5. Borisenko, V.E.; Ossicini, S. *What is What in the Nanoworld: A Handbook on Nanoscience and Nanotechnology*; John Wiley & Sons: New York, NY, USA, 2004.
6. Szostak, R. *Handbook of Molecular Sieves*; Van Nostrand Reinhold: New York, NY, USA, 1992.
7. Nguyen, S.V.; Szabo, V.; Trong On, D.; Kaliaguine, S. Mesoporous silica supported $LaCoO_3$ perovskites as catalysts for methane oxidation. *Microporous Mesoporous Mater.* **2002**, *54*, 51-61.
8. Umbarkar, S.B.; Kotbagi, T.V.; Biradar, A.V.; Pasricha, R.; Chanale, J.; Dongare, M.K.; Mamede, A.S.; Lancelot, C.; Payen, E. Acetalization of glycerol using mesoporous $MoO_3/SiO_2$ solid acid catalyst. *J. Mol. Catal. A Chem.* **2009**, *310*, 150-158.
9. Zhong, S.H.; Li, C.F.; Li, Q.; Xiao, X.F.; Supported mesoporous $SiO_2$ membrane synthesized by sol-gel-template technology. *Sep. Purif. Technol*. **2003**, *32*, 17-22.
10. Li, J.; Zhang, Y.; Hao, Y.; Zhao, J.; Sun, X.; Wang, L. Synthesis of ordered mesoporous silica membrane on inorganic hollow fiber. *J. Colloid Interface Sci.* **2008**, *326*, 439-444.
11. Liu, J.; Cai, Y.; Deng, Y.H.; Sun, Z.K.; Gu, D.; Tu, B.; Zhao, D. Magnetic 3-D ordered macroporous silica templated from binary colloidal crystals and its application for effective removal of microcystin. *Microporous Mesoporous Mater*. **2010**, *130*, 26-31.
12. Fukuoka, A.; Araki, H.; Sakamoto, Y.; Inagaki, S.; Fukushima, Y.; Ichikawa, M. Palladium nanowires and nanoparticles in mesoporous silica templates. *Inorg. Chim. Acta* **2003**, *350*, 371-378.
13. Choe, Y.S. New gas sensing mechanism for $SnO_2$ thin-film gas sensors fabricated by using dual ion beam sputtering. *Sens. Actuat. B* **2001**, *77*, 200-208.
14. Kim, D.; Yoon, J.; Park H.; Kim, K. $CO_2$-sensing characteristics of $SnO_2$ thick film by coating lanthanum oxide. *Sens. Actuat. B* **2000**, *62*, 61-66.

15. Hyodo, T.; Shimizu, Y.; Egashira, M. Design of mesoporous oxides as semiconductor gas sensor materials. *Electrochemistry* **2003**, *71*, 387-392.
16. Hyodo, T.; Nishida, N.; Shimizu, Y.; Egashira, M. Preparation and gas-sensing properties of thermally stable mesoporous $SnO_2$. *Sens. Actuat. B* **2002**, *83*, 209-215.
17. Sasahara, K.; Hyodo, T.; Shimizu, Y.; Egashira, M. Macroporous and nanosized ceramic films prepared by modified sol-gel method with PMMA microsphere templates. *J. Eur. Ceram. Soc*. **2004**, *24*, 1961-1967.
18. Hyodo, T.; Sasahara, K.; Shimizu, Y.; Egashira, M. Preparation of macroporous $SnO_2$ films using PMMA microspheres and their sensing properties to $NO_x$ and $H_2$. *Sens. Actuat. B* **2005**, *106*, 580-590.
19. Yuan, L.; Hyodo, T.; Shimizu, Y.; Egashira, M. Preparation of mesoporous and meso-macroporous $SnO_2$ powders and their application to $H_2$ gas sensor. *Sens. Mater.* **2009**, *21*, 241-250.
20. Supothina, S. Gas sensing properties of nanocrystalline $SnO_2$ thin films prepared by liquid flow deposition. *Sens. Actuat. B* **2003**, *93*, 526-530.
21. Firooz, A.A.; Hyodo, T.; Mahjoub, A.R.; Khodadadi, A.A.; Shimizu, Y.; Egashira, M. Synthesis and gas-sensing properties of nano- and meso-porous $MoO_3$-doped $SnO_2$. *Sens. Actuat. B* **2010**, *147*, 554-560.
22. Hyodo, T.; Abe, S.; Shimizu, Y.; Egashira, M. Gas-sensing properties of ordered mesoporous $SnO_2$ and effects of coatings thereof. *Sens. Actuat. B* **2003**, *93*, 590-600.
23. Szczuko, D.; Werner, J.; Oswald, S.; Behr, G.; Wetzig, K. Surface-related investigations to characterize different preparation techniques of Sb-doped $SnO_2$ powders. *Appl. Surf. Sci*. **2001**, *79*, 484-491.
24. Horrillo, M.C.; Serventi, A.; Rickerby, D.; Gutierrez, J. Influence of tin oxide microstructure on the sensitivity to redactor gases. *Sens. Actuat. B* **1999**, *58*, 474-477.
25. Jones, A.; Jones, T.A.; Mann, B.; Firth, J.G. The effect of the physical form of the oxide on the conductivity changes produced by $CH_4$, CO and $H_2O$ on ZnO. *Sens. Actuat.* **1984**, *5*, 75-88.
26. Xu, C.N.; Tamaki, J.; Miura, N.; Yamazoe, N. Grain size effects on gas sensitivity of porous $SnO_2$-based elements. *Sens. Actuat. B* **1991**, *3*, 147-155.
27. Ahn, J.P.; Kim, S.H.; Park, J.K.; Huh, M.Y. Effect of orthorhombic phase on hydrogen gas sensing property of thick film sensors fabricated by nanophase tin dioxide. *Sens. Actuat. B* **2003**, *7106*, 1-7.
28. Clifford, P.K.; Tuma, D.T. Characteristics of semiconductor gas sensors. II. Transient response to temperature change. *Sens. Actuat.* **1982**, *3*, 255-265.
29. Yamazoe, N.; Sakai, G.; Shimanoe, K. Oxide semiconductor gas sensors. *Catal. Surv. Asia* **2003**, *7*, 63-75.
30. Ahna, J.P.; Kim, J.H.; Park, J.K.; Huh, M.Y. Microstructure and gas-sensing properties of thick film sensor using nanophase $SnO_2$ powder. *Sens. Actuat. B* **2004**, *99*, 18-24.
31. Williams, G.; Coles, G.S.V. Gas-sensing potential of nanocrystalline tin dioxide produced by a laser ablation technique. *MRS Bull*. **1999**, *24*. 25-29.
32. Tholen, A.R. Formation land observation of ultrafine particles. *Mater. Sci. Eng*. **1993**, *A168*, 131-135.

33. Herrmann, J.M.; Disdier, J.; Fernandez, A.; Jimenez, V.M.; Sanchez-Lopez, J.C. Oxygen gas sensing behavior of nanocrystalline tin oxide prepared by the gas phase condensation method. *Nano Struct. Mater.* **1997**, *6*, 675-686.
34. Li, G.J.; Kawi, S. High-surface area $SnO_2$: A novel semiconductor oxide gas sensor. *Mater. Lett.* **1998**, *34*, 99-102.
35. Shimizu, Y.; Hyodo, T.; Egashira, M. Mesoporous semiconducting oxides for gas sensor application. *J. Eur. Ceram. Soc.* **2004**, *34*, 1389-1398.
36. Hieda, K.; Hyodo, T.; Shimizu, Y.; Egashira, M. Preparation of porous tin dioxide powder by ultrasonic spray pyrolysis and their application to sensor materials. *Sens. Actuat. B* **2008**, *133*, 144-150.
37. Hyodo, T.; Baba, Y.; Wada, K.; Shimizu, Y.; Egashira, M. Hydrogen sensing properties of $SnO_2$ varistors loaded with $SiO_2$ by surface chemical modification with diethoxydimethylsilane. *Sens. Actuat. B* **2000**, *64*, 175-181.
38. Li, L.L.; Mao, L.; Duan, X.C. Solvothermal synthesis and characterization of Sb-doped $SnO_2$ nanoparticles used as transparent conductive films. *Mater. Res. Bull.* **2006**, *41*, 541-546.
39. Wang, Y.D.; Chen, T. Nonaqueous and template-free synthesis of Sb doped $SnO_2$ microspheres and their application to lithium-ion battery anode. *Electrochim. Acta* **2009**, *54*, 3510-3515.
40. Kong, J.; Deng, H.; Yang, P.; Chu, J. Properties of pure and antimony-doped tin dioxide thin films fabricated by sol-gel technique on silicon wafer. *Mater. Chem. Phys.* **2009**, *114*, 854-859.